# Understanding the low resistivity of the amorphous phase of $Cr_2Ge_2Te_6$ phase-change material: Experimental evidence for the key role of Cr clusters

Shogo Hatayama,[1,2,*] Keisuke Kobayashi,[3,4] Yuta Saito,[2] Paul Fons,[2,5] Yi Shuang,[1] Shunsuke Mori,[1] Alexander V. Kolobov,[2,6] and Yuji Sutou[1,†]

[1]*Department of Materials Science, Graduate School of Engineering, Tohoku University, 6-6-11, Aoba-yama, Aoba-ku, Sendai 980-8579, Japan*
[2]*Device Technology Research Institute, National Institute of Advanced Industrial Science and Technology (AIST), Tsukuba Central 2, Umezono 1-1-1, Tsukuba 305-8568, Japan*
[3]*Materials Sciences Research Center, Japan Atomic Energy Agency, 1-1-1 Kouto, Sayo-cho, Hyogo 679-5148, Japan*
[4]*Research Institute of Kochi University of Technology, Tosa yamada, Kami City, Kochi 782-8502, Japan*
[5]*Department of Electronics and Electrical Engineering, Faculty of Science and Technology, Keio University, 3-14-1, Hiyoshi, Kohoku-ku, Yokohama 223-8522, Japan*
[6]*Department of Physical Electronics, Faculty of Physics, Herzen State Pedagogical University of Russia, 48 Moika Embankment, St. Petersburg 191186, Russia*

(Received 28 February 2021; revised 13 July 2021; accepted 21 July 2021; published 11 August 2021)

Different from the prototypical elemental semiconductors such as Si and Ge, chalcogenide-based phase-change materials (PCMs) generally show very high resistivity contrast between the amorphous and crystalline phases. In contrast to conventional PCMs, such as Ge-Sb-Te alloys, where the amorphous phase possesses higher resistivity, $Cr_2Ge_2Te_6$ (CrGT) exhibits the opposite dependence. Namely, the amorphous phase is characterized by a lower resistivity than the crystalline phase. Although density functional theory calculations suggest that Cr clusters are responsible for the low resistivity of amorphous CrGT, the effects of composition on the electrical properties have yet to be investigated. In this work, the dependence of the electrical properties on Cr content and the role of the Cr clusters were investigated experimentally using Hall effect, hard x-ray photoelectron spectroscopy (HAXPES), and optical property measurements. The electrical properties were found to be dependent on the Cr content. From a HAXPES core-level spectra analysis, it was found that the increased carrier density correlated with the extent of Cr clusters, indicating that the hole carriers present likely originated from Cr clusters. The increased concentration of Cr clusters was also found to lead to a shift of the valence band edge toward the Fermi level as well as to a decrease in the optical band gap. It has been suggested that the Cr clusters may induce the formation of new energy states close to the valence band edge. These results indicate that the Cr clusters play an essential role in determining the electrical properties of amorphous CrGT, and that tuning the film composition is an effective way to optimize device properties for nonvolatile memory applications.

DOI: 10.1103/PhysRevMaterials.5.085601

## I. INTRODUCTION

Phase-change materials (PCMs) show a large difference in their physical properties such as electrical resistivity between the high-resistance amorphous and low-resistance crystalline phases [1,2], although this is not the case for prototypical element semiconductors such as Si and Ge [3,4]. The large electrical contrast between the two phases enables PCM to be utilized for nonvolatile memory applications such as phase-change random access memory (PCRAM). Since PCRAM offers much faster operation speeds than flash memory and larger capacity than dynamic random access memory (DRAM), it has been proposed for storage-class memory (SCM) applications, a memory class which mitigates the large performance gap between storage (flash) and main memory (DRAM) [5]. Meanwhile, the operational energy requirements of conventional PCRAM devices have raised concern. In PCRAM, the data write/erase processes are carried out by Joule heating induced by electrical pulses, allowing reversible phase transitions between the amorphous and crystalline phases. In the amorphization process, the PCM is heated above the melting point to enable the melt-quench process, thus the operating power of PCRAM is dominated by the amorphization process. Since the crystalline phase in conventional PCMs as represented by prototypical $Ge_2Sb_2Te_5$ (GST) exhibits low resistivity in the crystalline phase, a large current is required for the amorphization process concomitantly leading to large operating power requirements.

To reduce the high power consumption of PCRAM, Hatayama *et al.* have proposed a $Cr_2Ge_2Te_6$ (CrGT) as a PCM [6,7]. CrGT is a layered material with rhombohedral $R\bar{3}$ symmetry [8]. Te atoms form a hexagonally closed packed structure with van der Waals gaps. Two-thirds of the octahedral sites formed by Te atoms are occupied by

*shogo-hatayama@aist.go.jp
†ysutou@material.tohoku.ac.jp

 ©2021 American Physical Society

TABLE I. Composition of the amorphous CrGT films.

| | Sample 1 | Sample 2 | Sample 3 | Sample 4 | Sample 5 |
|---|---|---|---|---|---|
| Cr content (at. %) | $13.7 \pm 0.5$ | $15.8 \pm 0.5$ | $17.3 \pm 0.5$ | $18.5 \pm 0.5$ | $20.6 \pm 0.5$ |
| Ge content (at. %) | $25.2 \pm 0.3$ | $24.6 \pm 0.3$ | $24.2 \pm 0.3$ | $23.8 \pm 0.3$ | $23.2 \pm 0.3$ |
| Te content (at. %) | $61.1 \pm 0.4$ | $59.6 \pm 0.4$ | $58.5 \pm 0.4$ | $57.7 \pm 0.4$ | $56.2 \pm 0.4$ |

Cr atoms, and the remaining octahedral sites are occupied by Ge-Ge dimers [8]. Different from conventional PCMs, CrGT shows an inverse resistance change between the high-resistance crystalline and low-resistance amorphous phases [6,9]. CrGT-based memory devices have been demonstrated to offer lower operating energy, faster operation speeds, and longer data retention over conventional GST-based devices [6,10]. In particular, the high-resistance crystalline phase was found to be essential to realize ultralow-energy amorphization. The origin of the high-resistance of crystalline CrGT has been studied in terms of the electronic structure, local atomic structure, and conduction mechanism [11–13]. It has been suggested that the likely origin of carrier generation in crystalline CrGT is Cr vacancies [11]. In recent studies, the current authors showed that the CrGT crystalline phase just after crystallization has a large number of Cr vacancies, and further heating results in the vacancies being filled by Cr atoms from the Cr clusters originally present in the amorphous phase, leading to an increase in resistivity [11]. Furthermore, in crystalline CrGT, two different conduction mechanisms, namely band and nearest-neighbor hopping conduction, were reported to coexist [12]. The carrier localization induced by local structural differences due to the presence of Cr clusters results in nearest-neighbor hopping conduction which lowers the mobility, leading to the high resistivity of the crystalline phase and low resistance-drift characteristics [12,14].

The electrical characteristics of amorphous CrGT have been studied as well [9,11]. One of the most intriguing features of amorphous CrGT is that the Fermi level ($E_F$) is located near the valence band maximum (VBM) [11]. It is reported that conventional chalcogenide glasses contain pairs of donorlike and acceptorlike chalcogen defects called valence alternation pairs (VAPs) [15–17]. Nearly equivalent amounts of these defects with different polarities compensate each other, leaving the $E_F$ pinned near the center of the band gap and leading to high resistivity [15,16]. In general, the acceptorlike defects are slightly more stable compared to donorlike defects, leading to the *p*-type semiconductor characteristics observed in many amorphous chalcogenides [15,16]. The small energy difference between $E_F$ and VBM in amorphous CrGT facilitates the excitation of hole carriers into the valence band more easily, resulting in unusually low resistivity [9]. However, the reasons why $E_F$ is located near the VBM in amorphous CrGT are still not clear, and an understanding the underlying mechanism behind the detailed electronic structure of transition-metal (TM) based PCMs will contribute to the development of novel materials for future PCRAM applications.

In previous hard x-ray studies [11] supported by density functional theory (DFT) calculations [18], it was argued that Cr clusters are present in amorphous CrGT. Furthermore, the volume fraction of the Cr clusters was found to decrease as crystallization progressed [11]. As mentioned above, the disappearance of Cr vacancies in crystalline CrGT upon heating is thought to originate from filling of the Cr vacancies by Cr atoms diffusing from Cr clusters [11]. Xu *et al.* also confirmed the presence of Cr clusters in the amorphous phase by DFT calculations results and pointed out that Cr clusters play an important role in carrier generation and in determining the location of $E_F$ in amorphous CrGT [18]. If this speculation is true, the electrical properties of amorphous CrGT film should exhibit a dependence on the Cr content, i.e., the volume fraction of the Cr clusters. In this study, we experimentally reveal the role of the Cr clusters in amorphous CrGT and the origin of its unusually low resistivity by measuring the dependence of the electrical properties of CrGT using Hall effect measurements, hard x-ray photoelectron spectroscopy (HAXPES), and optical band-gap measurement as a function of the Cr content.

## II. EXPERIMENTAL PROCEDURES

CrGT films were deposited on $SiO_2$ (100 nm)/Si or glass substrates using radio-frequency magnetron co-sputtering of Cr (99.9%), Ge (99.99%), and Te (99.99%) pure metal targets. The base pressure of the chamber was below $5.0 \times 10^{-5}$ Pa. The film composition was measured by Rutherford backscattering spectroscopy (RBS). For the RBS measurements, 30-nm-thick CrGT films were prepared on $SiO_2$/Si substrates using different Cr target sputtering power while fixing the power applied to the Ge and Te targets. To evaluate the dependence of the electrical properties on the Cr content in amorphous CrGT, five samples with different Cr content were prepared. The compositions of the obtained films are summarized in Table I showing that films with different Cr content were successfully fabricated by controlling the sputtering power with all films having almost the same Ge:Te ratio. A capping layer was grown on the CrGT film to prevent oxidation. The $SiO_2$ or Si-N layers were deposited depending on the experiments using a $SiO_2$ alloy target and by reactive sputtering of a Si (99.999%) pure target with $N_2$ flow, respectively.

The as-deposited CrGT films deposited on glass substrates were heated to 360 °C at a heating rate of 10 °C min$^{-1}$ followed by cooling to room temperature. Subsequently, the crystal structures of the as-deposited and annealed CrGT films were evaluated by x-ray diffraction (XRD) at room temperature using Cu $K\alpha 1$ and $K\alpha 2$ radiation in the conventional $2\theta/\theta$ Bragg-Brentano geometry (Rigaku, ULTIMA).

The resistivity and Hall properties for the CrGT films were measured using the van der Pauw method and AC Hall effect measurement (Toyo Corporation, ResiTest 8400), respectively. The temperature dependence of the carrier density was measured in He atmosphere in the temperature range

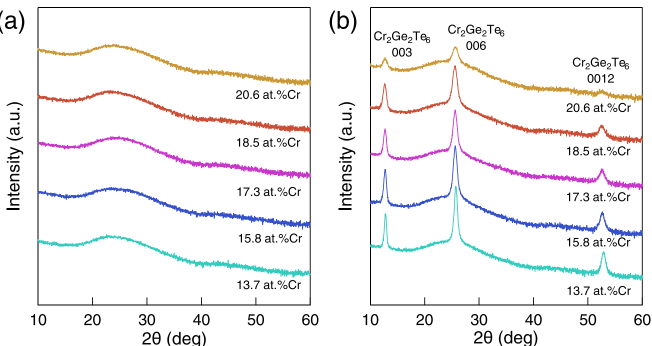


FIG. 1. XRD patterns of as-deposited (a) and annealed (b) CrGT films.

300–400 K with a step of 20 K. For these measurements, 100-nm-thick CrGT films were deposited on glass substrates with a 5-nm-thick $SiO_2$ capping layer.

HAXPES measurements were carried out at beamline BL47XU at SPring-8 (JASRI) on the amorphous CrGT films. For the HAXPES measurements, 200-nm-thick CrGT films were deposited on $SiO_2$/Si substrates with various compositions as summarized in Table I; the films were capped by a 5-nm-thick Si-N layer. The samples were placed into an experimental chamber with a pressure below $1.0 \times 10^{-5}$ Pa. Photoelectron spectra were obtained using an R4000 electron analyzer (VG Scienta). The HAXPES measurements were performed using a photon energy of 7.94 keV at room temperature. The binding energy scale was calibrated by measuring the position of the Au $4f$ level of a gold reference sample.

The relative reflectance with respect to an Al reference mirror and the transmittance of the amorphous CrGT films were measured at room temperature in the wavelength range 400–1100 nm using a spectrophotometer (JASCO, V-630BIO). For these measurements, 100-nm-thick amorphous CrGT films were deposited on glass substrates followed by the deposition of a 5-nm-$SiO_2$ capping layer. The absorption coefficient was calculated based on the obtained reflectance and transmittance values. Subsequently the optical band gap for the amorphous CrGT films was determined using these values.

## III. RESULTS AND DISCUSSION

### A. Cr content dependence of the electrical properties of amorphous CrGT films

Figure 1 shows XRD patterns for as-deposited and 360 °C-annealed films. All as-deposited films were confirmed to be amorphous at room temperature, and crystallized to a $Cr_2Ge_2Te_6$ single phase upon annealing. The dependence of the electrical properties on the Cr content was investigated for these amorphous CrGT films. In general, it is difficult to obtain reliable Hall properties for localized system such as amorphous chalcogenides using a conventional Hall effect setup. However, the AC Hall measurement used in this study enabled Hall measurements by amplifying the Hall voltage signal by oscillation of the AC magnetic field and use of a lock-in amplifier [19]. It is noteworthy to mention that this Hall measurement technique allowed us to successfully investigate the dependence of the electrical properties on the Cr content for amorphous CrGT as follows. Figure 2 shows the electrical properties of the amorphous CrGT films as a function of Cr content. The resistivity ($\rho$) was found to decrease monotonically with increasing Cr content. Since the resistivity is inversely proportional to the product of the mobility ($\mu$) and carrier density ($n$) in a semiconductor, an increase in $\mu$ or $n$ with increasing Cr content can be assumed to contribute to the decrease in $\rho$. Next, to reveal the dominant contribution to $\rho$, Hall effect measurements were carried out. All films showed $p$-type semiconductor characteristics regardless of composition, as reported in previous studies [6,9]. The value of $\mu$ was found to increase from 0.09 to 0.18 $cm^2\,V^{-1}\,s^{-1}$ with increasing Cr content and the small value of $\mu$ indicates that carriers are localized [9]. Compared to the trend in $\mu$, the value of $n$ was found to increase significantly with increasing Cr content, thus, the observed decrease in $\rho$ is considered to be mainly due to an increase in $n$. Since both $\mu$ and $n$ increase, these results indicate that electron scattering by Cr clusters is negligible and the change in $\mu$ is dominated by phonon scattering as reported in other chalcogenide materials [20,21].

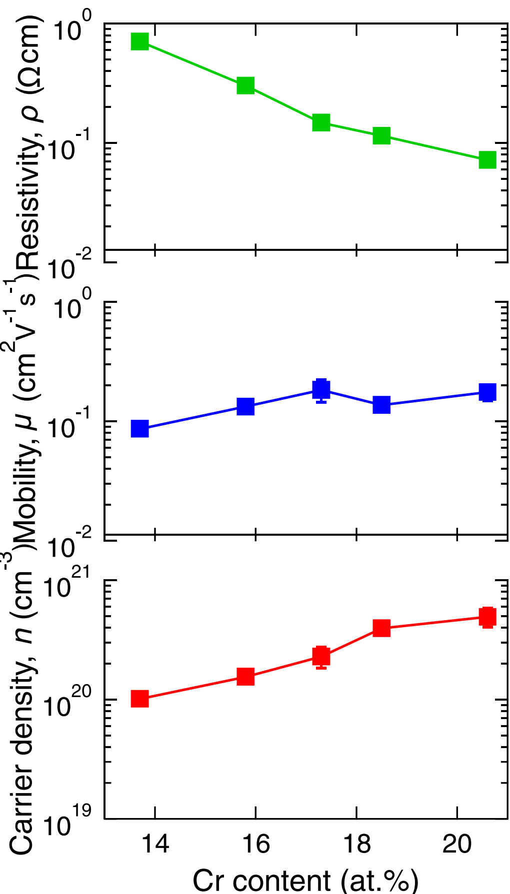


FIG. 2. The dependence of the resistivity, mobility, and carrier density on Cr content in amorphous CrGT. Error bars are comparable to symbol sizes.

Figure 3(a) shows the temperature dependence of $n$ for the CrGT films. All films showed an increase in $n$ with increasing temperature. Since an amorphous CrGT is known to show band conduction above room temperature [9], the

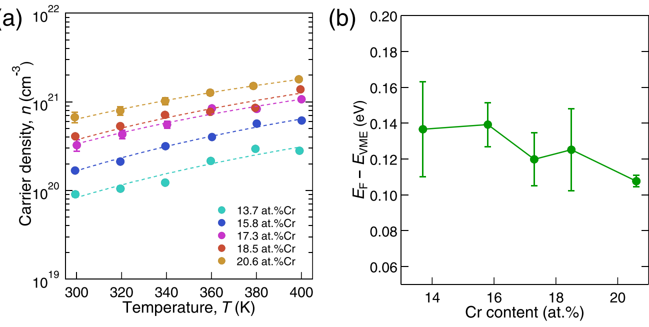


FIG. 3. (a) Temperature dependence of the carrier density of amorphous CrGT. The broken lines show a fit obtained using Eq. (1). Error bars are comparable to symbol sizes. (b) The location of the Fermi level relative to the mobility edge for the valence band ($E_F$–$E_{VME}$) as a function of Cr content.

temperature dependence of $n$ can be expressed by the following Eq. (1) [22]:

$$n = N_V \exp\left(-\frac{E_F - E_{VME}}{k_B T}\right), \tag{1}$$

where $N_V$ is the effective density of states in the valence band, and $E_F$–$E_{VME}$ describes the location of the $E_F$ with respect to the edge of extended states, referred to as the mobility edge for the valence band ($E_{VME}$). The obtained results could be well fit with Eq. (1), and estimated $E_F$–$E_{VME}$ values are shown in Fig. 3(b) as a function of Cr content. It can be seen that the quantity $E_F$–$E_{VME}$ tends to decrease with increasing Cr content. This indicates that the energy required to excite hole carriers becomes smaller, resulting in larger $n$ in a film with higher Cr content. Since the Ge:Te content ratio remains almost constant, as shown in Table I, these results suggest that the Cr content plays an important role in determining $n$ in amorphous CrGT.

### B. Determination of the optical band gap

Figures 4(a) and 4(b) show the reflectance ($R$) and transmittance ($T$) as a function of the wavelength for amorphous CrGT. In all films, the values of $R$ are 40–45% over the measurement wavelength range and all measured spectra are similar. The values of $T$ were found to monotonically decrease with decreasing wavelength in all films. In the higher wavelength region, $T$ was found to increase with decreasing Cr content, implying the presence of a corresponding increase in the optical band gap ($E_g$).

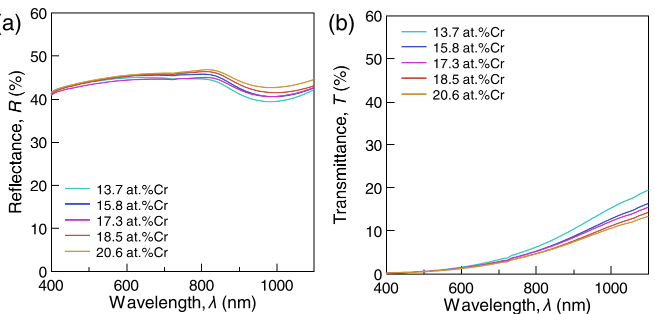


FIG. 4. Reflectance (a) and transmittance (b) spectra for amorphous CrGT as a function of wavelength.

To determine the $E_g$, the absorption coefficient ($\alpha$) was calculated using $R$, $T$, and the film thickness ($d$) based on the following Eq. (2) [23]:

$$\alpha = \frac{1}{d}\ln\left[\frac{(1-R)^2 + \{(1-R)^4 + 4R^2T^2\}^{1/2}}{2T}\right]. \tag{2}$$

Based on the calculated values of $\alpha$, $E_g$ was determined using Tauc plot assuming an indirect transition [24], as shown in Figs. 5(a)–5(e). Figure 6 shows the determined $E_g$ as a function of Cr content. In a CrGT film with 13.7 at. %Cr, $E_g$ was found to be 0.64 eV. With increasing Cr content, $E_g$ was found to decrease reaching a value of 0.54 eV in a CrGT film with 20.6 at. %Cr. For accurate estimation of $E_g$, the influence of thin-film interference should be considered to calculate $\alpha$. On the other hand, according to our previous work on the band gap of amorphous CrGT that explicitly took into account interference effects, the determined $E_g$ values were found to be comparable to the present work [9].

### C. Chemical bonding environment in amorphous CrGT

Xu *et al.* pointed out based upon DFT calculations that the hole carriers in the amorphous CrGT may originate from Cr clusters [18]. They assumed that the large coordination number of Cr in Cr clusters observed may result in there being insufficient valence electrons to form Cr-Cr bonds, resulting in the generation of hole carriers [18]. In fact, we experimentally confirmed using extended x-ray absorption fine structure (EXAFS) measurements that Cr clusters are present in as-deposited amorphous CrGT [11], but the detailed role that Cr clusters play in the reduction in the electrical resistivity has not been sufficiently understood. In our previous study, we determined the Cr-Cr bonds in the bulk originated from the Cr clusters seen in HAXPES spectra [11]. This earlier finding motivated us to evaluate the dependence of the bonding environment on Cr content to further understand the role that Cr clusters play in amorphous CrGT. To this end, we measured the Cr2$s$ and Te3$p_{3/2}$ core-level photoelectron spectra of the samples.

Figures 7(a) and 7(b) show HAXPES spectra for amorphous CrGT films with various Cr content. The inelastic background was subtracted using the Shirley method [25]. By fitting each experimental spectrum with Voigt functions, the measured peaks were deconvoluted into individual components. The Cr2$s$ peaks were deconvoluted into two peaks located at around 694.2–694.5 eV and around 697.8–698.2 eV, as shown in Fig. 7(a). The electronegativities of Cr, Ge, and Te are 1.56, 2.02, and 2.01, respectively [26], suggesting charge transfer from Cr to Te. Therefore, the peaks located at lower binding energies (yellow peaks) and higher binding energies (purple peaks) can be ascribed to the presence of Cr-Cr and Cr-Te bonds, respectively. The Te3$p_{3/2}$ spectra were also deconvoluted into two peaks located at around 818.2–818.4 eV and 819.3–819.4 eV. Due to the larger electronegativity difference of Cr-Te bonds compared to Ge-Te bonds, Te atoms participating in Cr-Te bonds are more electron rich than those participating in Ge-Te bonds. Therefore, the purple and red

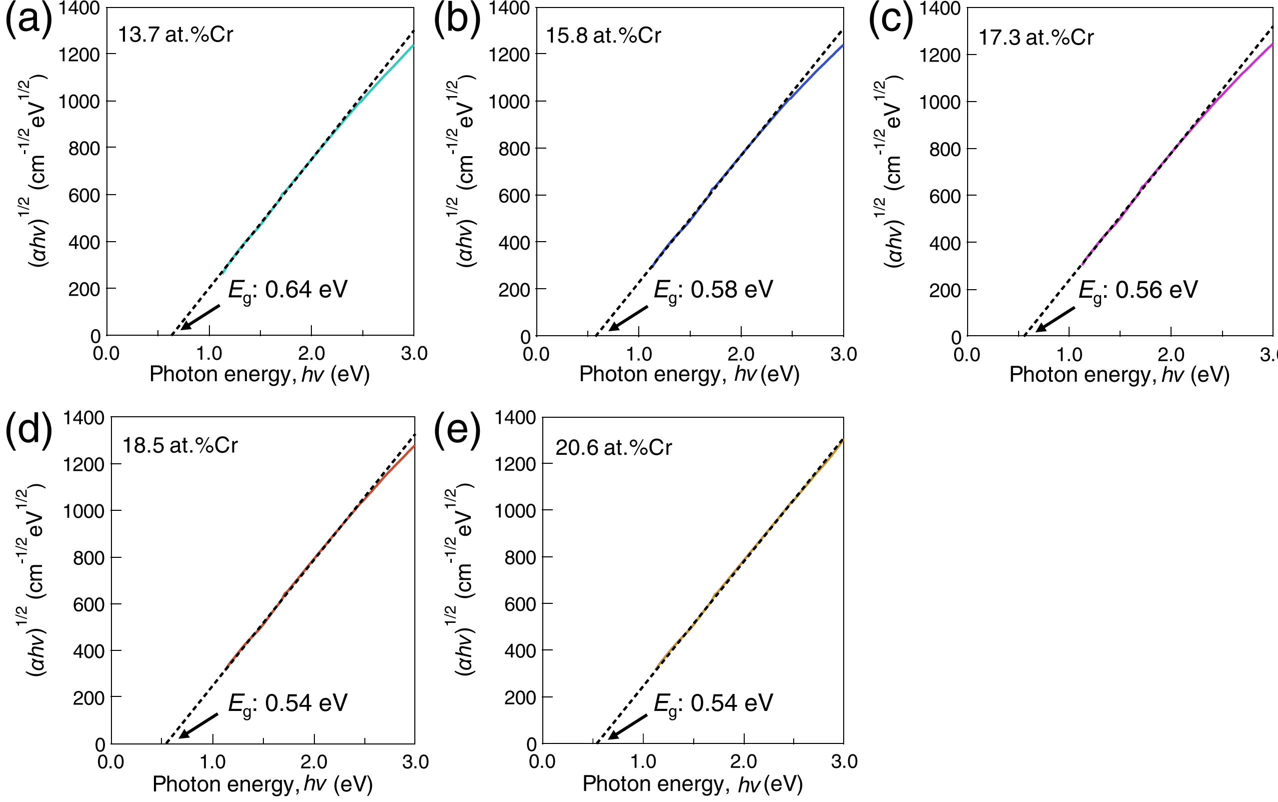


FIG. 5. Tauc plots for CrGT films with 13.7 at. % Cr (a), 15.8 at. % Cr (b), 17.3 at. % Cr (c), 18.5 at. % Cr (d), and 20.6 at. % Cr (e) as a function of phonon energy (solid lines) showing linear fits (dashed lines).

peaks shown in Fig. 7(b) can be ascribed to Cr-Te and Ge-Te bonds, respectively. Based on the peak analysis results, the area fraction of each bond as a function of Cr content was estimated, as shown in Fig. 8. It was found that the fraction of Cr-Te bonds was nearly independent of Cr content. Meanwhile, the fractions of Cr-Cr and Ge-Te bonds were found to linearly increase and decrease with increasing Cr content, respectively. In an amorphous CrGT film with 13.7 at. %Cr, Ge-Te bonds were dominant and decreased with increasing Cr content, while the opposite behavior was observed for Cr-Cr bonds. The fraction of Cr-Cr bonds becomes dominant in higher Cr content films, indicating that the number of Cr clusters increased. Combining the results shown in Figs. 2 and 8, the increase of $n$ can be associated with an increase in the number of Cr clusters, indicating that carrier generation originates from Cr clusters present in amorphous CrGT.

FIG. 6. Optical band gap of amorphous CrGT as a function of Cr content. Error bars are comparable to symbol sizes.

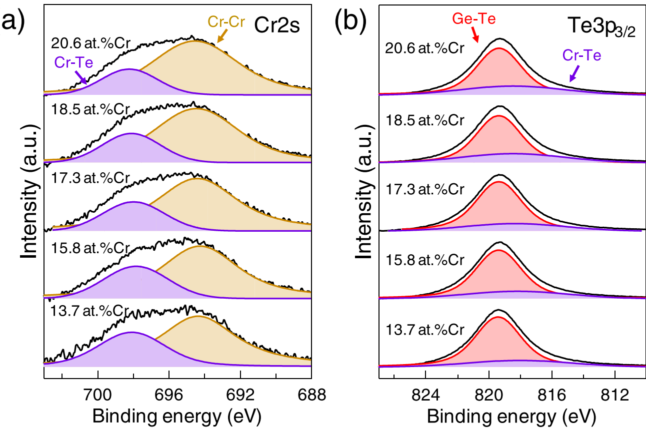


FIG. 7. (a) Cr2s and (b) Te3$p_{3/2}$ peaks obtained from HAXPES of amorphous CrGT. The purple, yellow, and red peaks are ascribed to Cr-Te, Cr-Cr, and Ge-Te bonds, respectively.

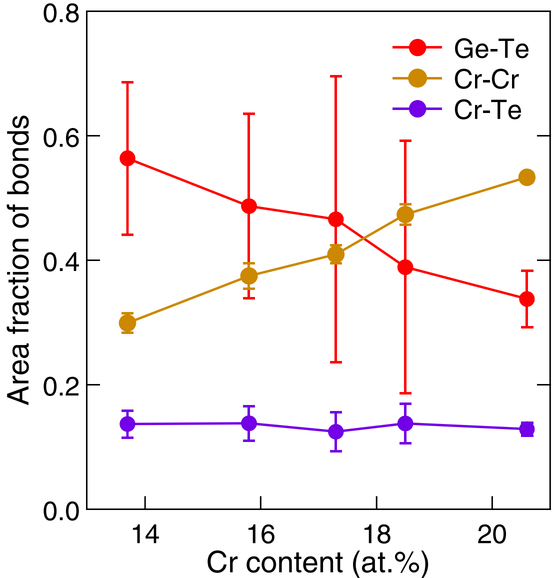


FIG. 8. Area fraction of Ge-Te (red), Cr-Cr (yellow), and Cr-Te bonds (purple) as a function of Cr content.

The obtained results are consistent with the DFT calculation reported by Xu *et al.* [18]. This suggests that the carrier generation mechanism present in amorphous CrGT is different from that active in conventional amorphous PCMs which originates from chalcogen defects.

### D. Valence band spectra of amorphous CrGT

The analysis of the HAXPES core-level spectra clearly indicates that the hole carriers originate from Cr clusters. However, the factors that determine the location of $E_F$ in amorphous CrGT, which leads to unusually low resistivity, are still not clear. To further investigate this issue, the valence band spectra of amorphous CrGT were measured as shown in Fig. 9(a). It can be seen from the zoomed-in image in the

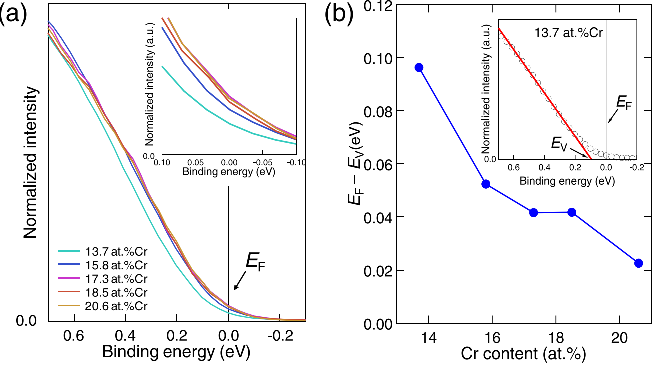


FIG. 9. (a) Cr content dependence of the valence band-edge spectra of amorphous CrGT. The inset is a zoomed-in image of the spectra in the vicinity of the Fermi level. The black solid line indicates the Fermi level. (b) The location of the Fermi level relative to valence band maximum ($E_F - E_V$) as a function of Cr content. The inset represents the linear fit used to determine the valence band maximum in the CrGT film with 13.7 at. % Cr.

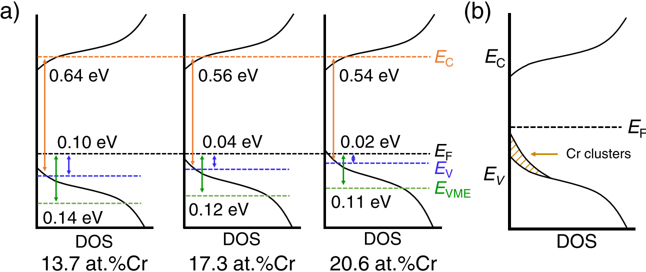


FIG. 10. (a) Schematic image showing the evolution of the band structure in amorphous CrGT for different Cr content. $E_C$, $E_F$, $E_V$, and $E_{VME}$ indicate the conduction band minimum, the Fermi level, the valence band maximum, and the mobility edge for the valence band, respectively. (b) Schematic image of the band structure for amorphous CrGT. The shaded area indicated by yellow solid lines indicates the density of states ascribed to the Cr clusters.

inset that the spectral edge shifts toward lower binding energies with increasing Cr content. The intensity of the valence band spectra at $E_F$ (binding energy = 0 eV) was also found to increase with the edge shift. Based on the result shown in Fig. 9(a), the location of the VBM ($E_V$) was determined by linear fitting, as shown in the inset of Fig. 9(b) [27,28]. The position of $E_F$ relative to $E_V$ ($E_F - E_V$) as a function of Cr content was estimated, as shown in Fig. 9(b). The value of $E_F - E_V$ in amorphous CrGT with 13.7 at. %Cr was found to be 0.096 eV, which then decreased with increasing Cr content. Finally, $E_F - E_V$ reached the value of 0.023 eV for a film with 20.6 at. %Cr.

The results shown in Figs. 3(b) and 9(b) suggest that the location of $E_F$ approached the valence band maximum with increasing Cr content. There are two possible mechanisms to explain this phenomenon. One is that the $E_F$ is not pinned in the band gap and moves toward the valence band in the presence of hole carrier doping. The other is that the $E_F$ is pinned in the band gap and the valence band tail shifts toward the $E_F$ due to the formation of new states originated from the Cr clusters. The decrease in $E_g$, as shown in Fig. 6, is assumed to be a consequence of the extension of valence or conduction band tails. Meanwhile, an analysis of the valence band spectra revealed that $E_F - E_V$ decreased by 0.073 eV. Since the decrease in $E_g$ is comparable to that in the $E_F - E_V$, the decrease in $E_g$ with increasing Cr content is attributed to the extension of the valence band tail.

The evolution of the band structure in the amorphous CrGT films with different Cr content has been schematically depicted based on the aforementioned discussion and is shown in Fig. 10(a). The change in the density of states (DOS) distribution for the valence band determines the overall electronic structure of amorphous CrGT. From core-level measurements, only the fraction of Cr-Cr bonds related to the Cr clusters increases with increasing Cr content. Therefore, the change in the DOS in the valence band tail is assumed to be induced by the presence of Cr clusters. We note here that a change in the DOS distribution near the VBM due to TM clusters (TM: Pd) has been also reported in mordenite by Grybos *et al.* [29]. To explain this phenomenon, a schematic of the band structure for amorphous CrGT has been depicted in Fig. 10(b). $E_F$ is assumed to be located near the center of the band gap

in the intrinsic band structure of amorphous CrGT as well as conventional amorphous PCMs. However, in CrGT, Cr atoms form clusters, and the new states originating from the Cr clusters are created in addition to the original electronic structure. Even though $E_F$ is pinned in midgap and is not easily moved, the newly formed states effectively decrease the energy difference between the $E_F$ and valence band in amorphous CrGT. As a consequence, decreases in $E_F$–$E_{VME}$, $E_g$ ($E_C - E_V$), and $E_F - E_V$ were observed as shown in Figs. 3(b), 6 and 9(b), respectively. Such formation of new states is also consistent with the observed increase in the intensity of the valence band spectra, as shown in Fig. 9(a). This implies that $E_F$ in amorphous CrGT is intrinsically pinned, but the location of $E_F$ relative to the valence band maximum is tunable by the introduction of the Cr cluster-related states. The obtained results explain the role of Cr clusters in carrier generation and the location of the $E_F$ that determines the electrical properties of the amorphous CrGT such as its abnormally low resistivity.

In classical theory, the electrical properties of amorphous chalcogenides are considered to be insensitive to doping [16]. Meanwhile, relatively high doping concentrations of TM elements are empirically known to lower the resistivity of amorphous PCMs [30–33]. Since the main purpose of TM doping of amorphous PCMs is to enhance thermal stability as well as to accelerate crystallization speed [30–35], the origin of the lowering resistivity has not attracted much attention. On the other hand, recent studies have uncovered excellent characteristics of TM-doped PCMs, e.g., Ti-$Sb_2Te_3$, Sc-$Sb_2Te_3$, and Sn-$Sb_7Te_3$ [34–36] and TM compound-type PCMs, e.g., CrGT and $Cu_2GeTe_3$ [6,37,38]. Therefore, the origins of their electrical characteristics in the amorphous phase must be understood. Among TM-included PCMs, in particular, compound-type PCMs show quite low resistivity values in their amorphous phases. For instance, the resistivity values of CrGT, $Cu_2GeTe_3$, and FeTe in their amorphous phases were reported to be $2.2 \times 10^{-1}\,\Omega\,\mathrm{cm}$, $2.0\,\Omega\,\mathrm{cm}$, and $1.3 \times 10^{-3}\,\Omega\,\mathrm{cm}$, respectively [6,39,40]. Compared to the resistivity values for the amorphous phase of conventional PCMs such as $Ge_2Sb_2Te_5$ ($2.2 \times 10^3\,\Omega\,\mathrm{cm}$) and GeTe ($1.7$–$2.5 \times 10^3\,\Omega\,\mathrm{cm}$) [39,41], the resistivity values of these three amorphous PCMs are much lower. It is noteworthy that the existence of TM clusters was reported for all of the above, namely amorphous CrGT, $Cu_2GeTe_3$, and FeTe films [11,40,42,43]. These facts suggest that in amorphous PCMs with a relatively high concentration of TM element, the formation of TM cluster-originated new states near the VBM leads to dramatic decreases in the resistivity of the amorphous phase.

## IV. CONCLUSION

Electrical, optical, and HAXPES measurements were carried out on amorphous CrGT to understand the mechanism of Cr cluster-induced low resistivity. The resistivity was found to decrease due to an increase in the carrier density with increasing Cr content. Core-level photoelectron measurements indicated that Cr-Cr bonds become dominant in amorphous CrGT with high Cr content, leading to an increase in the number of Cr clusters. Both the valence band spectra and optical band gap were found to depend on the Cr content. With increasing Cr content, the valence band tail expands towards the center of the band gap due to the formation of new states attributed to Cr clusters, indicating that the relative position of the Fermi level moves closer to the VBM. In contrast to the general trend, in which carrier generation in amorphous PCMs originates from chalcogen defects, the results obtained here demonstrate that Cr clusters are the origin of the carrier generation and play a key role in determining the electrical properties of amorphous CrGT. These findings are expected to provide valuable insights of possible mechanisms to lower the resistivity of TM-based amorphous PCMs, and will aid in the development of novel PCMs for nonvolatile memory applications.

## ACKNOWLEDGMENTS

This work was supported by KAKENHI (Grants No. 18H02053 and No. 19H02619). A.V.K. would like to acknowledge partial support of this work by the Ministry of Education of the Russian Federation (Project No. FSZN-2020-0026). The HAXPES measurement was performed at beamline BL01B1 at SPring-8, Japan as part of Proposal No. 2020A1240.

[1] M. Wuttig and N. Yamada, Nat. Mater. **6**, 824 (2007).

[2] H.-S. P. Wong, S. Raoux, S. Kim, J. Liang, J. P. Reifenberg, B. Rajendran, M. Asheghi, and K. E. Goodson, Proc. IEEE **98**, 2201 (2010).

[3] M. H. Brodsky, R. S. Title, K. Weiser, and G. D. Pettit, Phys. Rev. B **1**, 2632 (1970).

[4] T. T. Tran, J. Wong-Leung, L. A. Smillie, A. Hallén, M. G. Grimaldi, and J. M. Williams, arXiv:1908.08246.

[5] S. W. Fong, C. M. Neumann, and H. P. Wong, IEEE Trans. Electron Devices **64**, 4374 (2017).

[6] S. Hatayama, Y. Sutou, S. Shindo, Y. Saito, Y. H. Song, D. Ando, and J. Koike, ACS Appl. Mater. Interfaces **10**, 2725 (2018).

[7] S. Hatayama, Y. Sutou, D. Ando, and J. Koike, MRS Commun. **8**, 1167 (2018).

[8] V. Carteaux, D. Brunet, G. Ouvrard, and G. André, J. Phys.: Condens. Matter **7**, 69 (1995).

[9] S. Hatayama, Y. Sutou, D. Ando, J. Koike, and K. Kobayashi, J. Phys. D: Appl. Phys. **52**, 105103 (2019).

[10] S. Hatayama, Y. Abe, D. Ando, and Y. Sutou, Phys. Status Solidi RRL **15**, 2000392 (2021).

[11] S. Hatayama, Y. Shuang, P. Fons, Y. Saito, A. V. Kolobov, K. Kobayashi, S. Shindo, D. Ando, and Y. Sutou, ACS Appl. Mater. Interfaces **11**, 43320 (2019).

[12] S. Hatayama, T. Yagi, and Y. Sutou, Results Mater. **8**, 100155 (2020).

[13] Y. Saito, S. Hatayama, Y. Shuang, P. Fons, A. V. Kolobov, and Y. Sutou, Sci. Rep. **11**, 4782 (2021).

[14] S. Hatayama, Y.-H. Song, and Y. Sutou, Mater. Sci. Semicond. Process. **133**, 105961 (2021).

[15] A. Pirovano, A. L. Lacaita, A. Benvenuti, F. Pellizzer, and R. Bez, IEEE Trans. Electron Devices **51**, 452 (2004).
[16] *Electronic Process in Non-Crystalline Materials*, edited by N. F. Mott and E. A. Davis (Clarendon, Oxford, 1979).
[17] A. V. Kolobov, P. Fons, and J. Tominaga, Sci. Rep. **5**, 13698 (2015).
[18] M. Xu, Y. Guo, Z. Yu, K. Xu, C. Chen, H. Tong, X. Cheng, M. Xu, S. Wang, C. Z. Wang, K.-M. Ho, and X. Miao, J. Mater. Chem. C **7**, 9025 (2019).
[19] A. J. E. Rettie, H. C. Lee, L. G. Marshall, J.-F. Lin, C. Capan, J. Lindemuth, J. S. McCloy, J. Zhou, A. J. Bard, and C. B. Mullins, J. Am. Chem. Soc. **135**, 11389 (2013).
[20] D. Errandonea, A. Segura, J. F. Sánchez-Royo, V. Muñoz, P. Grima, A. Chevy, and C. Ulrich, Phys. Rev. B **55**, 16217 (1997).
[21] J. F. Sánchez-Royo, D. Errandonea, A. Segura, L. Roa, and A. Chevy, J. Appl. Phys. **83**, 4750 (1998).
[22] *Physics of Semiconductor Devices*, 3rd ed., edited by S. M. Sze and K. K. Ng (Wiley, New York, 2007).
[23] R. Vahalová, L. Tichý, M. Vlček, and H. Tichá, Phys. Status Solidi A **181**, 199 (2000).
[24] J. Tauc, R. Grigorovici, and A. Vancu, Phys. Status Solidi **15**, 627 (1966).
[25] D. A. Shirley, Phys. Rev. B **5**, 4709 (1972).
[26] A. L. Allred and E. G. Rochow, J. Inorg. Nucl. Chem. **5**, 264 (1958).
[27] S. A. Chambers, T. Droubay, T. C. Kaspar, M. Gutowski, and M. Van Schilfgaarde, Surf. Sci. **554**, 81 (2004).
[28] S. A. Chambers, T. Droubay, T. C. Kaspar, and M. Gutowski, J. Vac. Sci. Technol. B **22**, 2205 (2004).
[29] R. Grybos, L. Benco, T. Bučko, and J. Hafner, J. Chem. Phys. **130**, 104503 (2009).
[30] Y. Lu, S. Song, Z. Song, F. Rao, L. Wu, M. Zhu, B. Liu, and D. Yao, Appl. Phys. Lett. **100**, 193114 (2012).
[31] S. Guo, Z. Hu, X. Ji, T. Huang, X. Zhang, L. Wu, Z. Song, and J. Chu, RSC Adv. **4**, 57218 (2014).
[32] Y. Zhu, Z. Zhang, S. Song, H. Xie, Z. Song, X. Li, L. Shen, L. Li, L. Wu, and B. Liu, Mater. Res. Bull. **64**, 333 (2015).
[33] L. Cao, X. Ji, W. Zhu, Q. She, Y. Chen, Z. Hu, S. Guo, Z. Song, F. Rao, B. Qian, and L. Wu, ECS Solid State Lett. **4**, P102 (2015).
[34] M. Zhu, M. Xia, F. Rao, X. Li, L. Wu, X. Ji, S. Lv, Z. Song, S. Feng, H. Sun, and S. Zhang, Nat. Commun. **5**, 4086 (2014).
[35] F. Rao, K. Ding, Y. Zhou, Y. Zheng, M. Xia, S. Lv, Z. Song, S. Feng, I. Ronneberger, R. Mazzarello, W. Zhang, and E. Ma, Science **358**, 1423 (2017).
[36] V. Bilovol, M. Fontana, J. A. Rocca, H. H. M. Chanduví, A. M. M. Navarro, A. V. G. Rebaza, L. A. Errico, A. Liang, D. Errandonea, and A. M. Ureña, J. Alloys Compd. **845**, 156307 (2020).
[37] T. Kamada, Y. Sutou, M. Sumiya, Y. Saito, and J. Koike, Thin Solid Films **520**, 4389 (2012).
[38] Y. Sutou, T. Kamada, M. Sumiya, Y. Saito, and J. Koike, Acta Mater. **60**, 872 (2012).
[39] S. Shindo, Y. Sutou, J. Koike, Y. Saito, and Y.-H. Song, Mater. Sci. Semicond. Process. **47**, 1 (2016).
[40] H. W. Ho, P. S. Branicio, W. D. Song, K. Bai, T. L. Tan, R. Ji, Y. Yang, P. Yang, Y. H. Du, and M. B. Sullivan, Acta Mater. **112**, 67 (2016).
[41] E. K. Chua, R. Zhao, L. P. Shi, T. C. Chong, T. E. Schlesinger, and J. A. Bain, Appl. Phys. Lett. **101**, 012107 (2012).
[42] K. Kobayashi, J. M. Skelton, Y. Saito, S. Shindo, M. Kobata, P. Fons, A. V. Kolobov, S. Elliott, D. Ando, and Y. Sutou, Phys. Rev. B **97**, 195105 (2018).
[43] J. R. Stellhorn, B. Paulus, S. Hosokawa, W. C. Pilgrim, N. Boudet, N. Blanc, H. Ikemoto, S. Kohara, and Y. Sutou, Phys. Rev. B **101**, 214110 (2020).